

See discussions, stats, and author profiles for this publication at: <https://www.researchgate.net/publication/264553366>

A Novel Low Reynolds Number Airfoil Design for Small Horizontal Axis Wind Turbines

Article in *Wind Engineering* · August 2014

DOI: 10.1260/0309-524X.38.4.377

CITATIONS

16

READS

1,814

3 authors, including:



Haseeb Shah

Universiti Brunei Darussalam

6 PUBLICATIONS 46 CITATIONS

[SEE PROFILE](#)



Sathyajith Mathew

Universiti Brunei Darussalam

41 PUBLICATIONS 1,203 CITATIONS

[SEE PROFILE](#)

A Novel Low Reynolds Number Airfoil Design for Small Horizontal Axis Wind Turbines

by

Haseeb Shah, Sathyajith Mathew and Chee Ming Lim

REPRINTED FROM

WIND ENGINEERING
VOLUME 38, No. 4, 2014

MULTI-SCIENCE PUBLISHING COMPANY
5 WATES WAY · BRENTWOOD · ESSEX CM15 9TB · UK
TEL: +44(0)1277 224632 · FAX: +44(0)1277 223453
E-MAIL: mscience@globalnet.co.uk · WEB SITE: www.multi-science.co.uk

A Novel Low Reynolds Number Airfoil Design for Small Horizontal Axis Wind Turbines

*Haseeb Shah, Sathyajith Mathew and Chee Ming Lim

Centre for Advanced Materials and Energy Sciences, Universiti Brunei Darussalam, Jalan Tingku link, BE1410, Brunei Darussalam.

E-mail: H.shah.nuua@hotmail.co.uk

Received 5/1/2014; Revised 1/3/2014; Accepted 13/3/2014

ABSTRACT

In order to improve the performance of small horizontal axis wind turbines at low wind speed, this study designs a novel airfoil section with an optimum transition ramp through multipoint inverse design method. A viscous analysis code is used to close the design loop. Further, Shear stress transport-transition model in ANSYS-Fluent is employed with modified constants to analyze the flow and aerodynamic performance of the airfoil at Reynolds numbers 60 000, 100 000, 200 000, 300 000 and 500 000. Next we consider the designing of a 2m rotor from the new airfoil section using an evolutionary algorithm for optimization. The power coefficient and self starting of a small 2m wind turbine is improved significantly with the chosen generator resistive torque of 0.5Nm, the new airfoil section and the optimization technique for finding the optimal values of the parameters.

Keywords: Low Re airfoil, small wind turbine, separation bubble, ANSYS-Fluent, multi objective optimization

I. INTRODUCTION

Electricity generation from wind turbines has increased very rapidly during the last decades and is projected to soar from 2.6% today to 18% of world's electricity production by 2050, according to International Energy Agency (IEA) [1]. In contrast to large horizontal axis wind turbines (HAWTs) in mega-watts (MW) range, small HAWTs are also considered to play major role in the future 'sustainable energy mix' in the forms of stand alone, grid connected, or building-integrated systems. Small HAWTs as defined by IEC 61400-2 [2] have a rotor swept area of no more than 200m² equivalent to power of about 50kW generating at voltage below 1000V AC or 1500V DC [2].

Compared to large HAWTs, Small HAWTs mainly due to their size, operate at low Reynolds number ($Re \leq 500\,000$) along the entire span of the blade. For simplicity reasons small machines are designed to rely on self startup [3–5]. Moreover, small HAWTs are often installed at locations where power generation is the necessity and these locations do not always have the best wind [5].

Two of the important factors that define the power output of small wind machines are: 1) Effective blade profile and 2) Early startup [5, 6]. The effectiveness of the blade mainly relies upon the airfoil employed along the span of the blade [6]. Moreover, it is desirable from an airfoil to produce higher values of Lift-to-drag ratios (L/D ratio) at moderate Lift coefficient (C_L). The starting (α_s) happens when the aerodynamic torque of the blades overcomes the resistive torque of the generator and can be mathematically expressed as:

$$\alpha_s = \frac{(Q - Q_r)}{J} \quad (1)$$

Where Q_r represents the resistive torque (measured in Nm) from the generator, Q is the torque produced by the blades and J is the rotor inertia [5]. From Eq.1 the starting performance of small HAWTs

*Corresponding Author: Haseeb Shah, Centre for Advanced Materials and Energy Sciences, Universiti Brunei Darussalam, Jalan Tingku link, BE1410, Brunei Darussalam H.shah.nuua@hotmail.co.uk

can be further improved by minimizing the total inertia of the rotor and increasing the aerodynamic torque from the blades. This is achievable by using a thin airfoil with light and durable material and higher aerodynamic performance. According to Wood [5] the aerodynamic torque on the starting blade can be calculated by generic flat plate expressions for the lift and the drag coefficients at higher angle of attacks (α). The role of resistive torque or the so called cogging torque from the generator cannot be neglected in starting performance and is preferred to be as low as possible [5]. Moreover, it is to note that the aerodynamic torque at starting accelerate the rotor instead of producing power.

Traditional airfoils designed for full-scale aircraft such as NACA and NASA series were designed mainly to operate at High ($Re > 3 \times 10^6$) and/or medium ($5 \times 10^5 < Re < 3 \times 10^6$) Re . Employment of such airfoils on small HAWTs are reported to exhibit poor performance due to laminar separation bubbles (LSB) at low Re [7] [8] [9]. Wide ranges of low Re airfoils documented in literature were particularly for free flight model aircrafts, heavy lift radio controlled aircraft and sail planes. [10–12]. A number of them have been considered and tested in wind tunnels for small HAWTs [7, 9, 13].

Studies have shown that low Re airfoils are required to be thin (chord thickness of 5%) which reduces the suction peak near the leading edge causing decrease in adverse pressure gradients (APG) on the upper surface of the airfoil [5, 8, 14]. An optimized airfoil with maximum thickness of 4% and C_L values ranging from 1.28, 1.38, 1.41 and 1.45 at $Re = 55\,000, 70\,000$ and $100\,000$ has been recently documented for small HAWT application [15]. SG00XX airfoil series (SG6040–SG6043) designed by Giguère and Selig [9] for small HAWT application with C_L values ranging from 1.4–1.65 operating in Re 100 000–500 000. S822 and S823 airfoils are thicker and were intended for small variable speed HAWTs with rated power between 1–5 kW [16]. BW-3 airfoil was also designed for 7 m, 10 kW small wind turbines by Bergey Wind Power [15]. The Six airfoils E387, FX63137, S822, S834, SD2030, and SH3055 were tested for a Re range of 100 000–500 000 by Selig and MacGranahan [13] for small HAWT application. So far airfoils exclusively designed for small HAWT are still limited. Moreover there is a lack of data for the Re range 10 000–100 000 [4, 5].

In an effort to improve the performance of a small HAWT, an airfoil is designed in an interactive and iterative fashion by multipoint inverse method in PROFOIL. The airfoil is designed to be used over the entire span of the blade or at least the tip region. A concise introduction to low Reynolds number aerodynamics is provided in section 2 in which approaches to attain low bubble drag are also discussed. Section 3 highlights the airfoil design. Initial aerodynamic performance of new airfoil simulated in viscous analysis code -Xfoil is described in section 4. Further in section 4, ANSYS-CFD method is used to simulate the flow behavior, transition location and aerodynamic performance of the new airfoil. In Section 5 a differential evolutionary optimization method is used to design and asses a 2 m small HAWT upon the employment of the new airfoil. Finally, conclusions are given in section 6.

2. LOW REYNOLDS NUMBER AIRFOIL AERODYNAMICS

Low Reynolds number airfoils and aerodynamics has been in interest of many aerodynamists for application in small wind turbines, micro-air unmanned vehicles and sailplanes [3–21]. Flows at $Re \leq 500\,000$ are generally governed by separation and reattachment in the attached boundary layer, forming laminar separation bubble (LSB). Such an LSB is mainly caused by inability of flow to transit to turbulent flow and rather separates; while the transition occurs in free shear layer as shown in Fig.1. LSBs are classified into long or short bubbles and their length is expressed in terms of airfoil chord (x/c). At Re 100 000 longer LSB is generally seen to cover up to 20–30% of upper surface of airfoil, whereas shorter LSB may form at higher Reynolds number [14].

Degradation of an airfoil performance by rapidly increasing the coefficient of drag (C_D) and degrading C_L is one of the main traits of LSB. According to Drela [17], skin friction drag can be expressed by von Kármán integral boundary layer equation:

$$\frac{1}{\rho u_e^2 \theta} \frac{d(\rho u_e^2 \theta)}{d\xi} = \frac{C_f}{2\theta} - \frac{H}{u_e} \frac{du_e}{d\xi} \quad (2)$$

Where, u_e is the boundary layer edge velocity, ξ is the boundary layer coordinates, H is the shape factor and θ is the momentum thickness. Skin friction C_f inside the bubble is almost zero, hence integral boundary condition becomes:

$$\frac{\Delta(\rho u_e^2 \theta)}{\rho u_e^2 \theta} \approx -H \frac{\Delta u_e}{u_e} \quad (3)$$

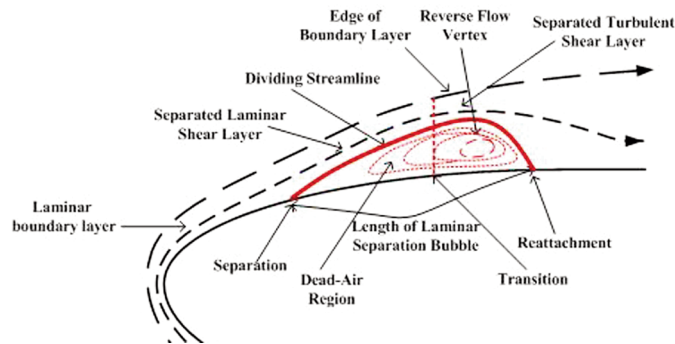


Figure 1. Schematic illustration of laminar separation bubble over airfoil suction surface [adapted from 24]

Where, total momentum defect $\rho u_e^2 \theta$, H and u_e can be considered as average quantities.

$$\Delta \rho u_e^2 \theta = -\rho u_e \delta^* \Delta u \quad (4)$$

Where, δ^* is the displacement thickness. Thus the increase in drag due to laminar separation bubble is proportional to the product of average mass defect $\rho u_e \delta^*$ and edge velocity jump Δu . The graphical illustration of this result is shown in Fig.2. Four edge velocity distributions are given with drag increment that grows downstream. Starting from case 4, no increase in drag is observed until the transition occurs, after which the drag increases rapidly. At separation and reattachment, a large drop in the edge velocity can be seen from larger jump in the drag increment, in this case the LSB is considered to be long. Whereas case 3 demonstrates rather smaller LSB, predicted from the smaller jump in the drag increment. Transition from laminar to turbulent flow is assumed to have occurred without the mechanism of LSB in case 1. Apparently, between these cases there surely exists an optimum bubble size and consequently an optimum transition location which can minimize the bubble drag increment and may be plotted as Case 2 in Fig.2. It is to be noted that additional factors such as Re and angle of attack are also main contributors in defining the proportion of LSB.

The need to control LSB for improved aerodynamic performance from airfoils has led to several approaches that can artificially trigger the transition [14, 17–19]. These includes the use of 1). Trip or mechanical tabulators, or 2). Certain amount of roughness, or 3). Transition ramp. The former methods can only be applied to existing airfoils, whereas, the latter method can be used in designing new airfoils [5, 6].

A transition ramp is basically a shallow, adverse pressure gradient introduced over either side of the airfoil. In the present case, only suction side transition ramp is considered (Fig.3). Such transition ramp stabilizes and promotes an effective transition from laminar to turbulent flow resulting in a smaller LSB and a softer stall. It is to emphasize that complete elimination of the LSB is also undesirable at low Re since it will clearly increase the skin friction drag, as seen in Fig 2-case 1. In order to gain high L/D ratios from a low Re airfoil, the transition is required to be delayed

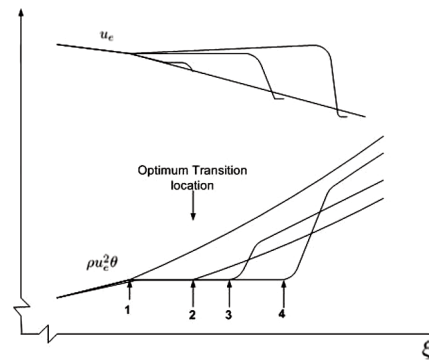


Figure 2. Effects of transition location on drag [adapted from 17]

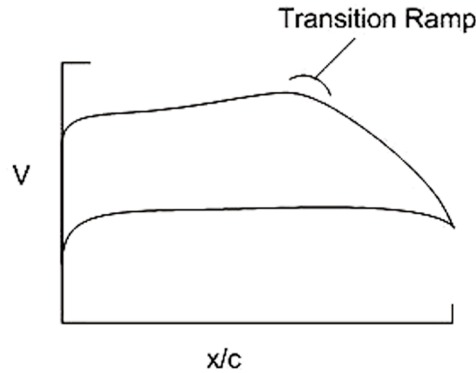


Figure 3. Concept of transition ramp [adapted from 18]

for as long as possible. Moreover, the size and shape of the transition ramp can be systematically tailored to outline the off-design performance by controlling the size of LSB. The optimum transition location in Fig.2 can possibly be attained from an airfoil having optimum transition ramp that surpass the LSB without increasing the thickness of the boundary layer [18]. Therefore a designer has to make a tradeoff between the operation performance (transition location and size of the LSB) and the shape and proportion of transition ramp.

3. AIRFOIL DESIGN

The best combination of airfoils geometric (maximum thickness, maximum camber, length of transition ramp, etc) and performance (L/D ratio, C_{Lmax} , etc) parameters are normally subjected to structural integrity, ease of manufacturing and total costs [13]. Thus, the decision of optimization of airfoil shape and performance completely relies on the objective of the designer and the ultimate solution must include some compromises [17]. From a practical standpoint, as small wind turbines mainly rely upon self starting using a thick airfoil section (in this case with higher transition ramp) may increase the total rotor inertia resulting in slow startup. Whereas, using a particular lighter material to overcome the total weight could affect the total cost of the machine. On the other hand, employing a very thin airfoil may result in structural problems because of the higher centrifugal loads on the blade in lower rated power [5]. In order to meet such aerodynamic and structural requirements of small HAWT, an airfoil shape with moderate thickness and higher aerodynamic performance is designed by multipoint inverse design method in PROFOIL [26, 27]. Such method is based on conformal mapping to transform the potential flow around circle into that around the airfoil. A simple example of designing airfoil geometry from conformal mapping is the Joukowski airfoil problem, fixing the mathematical transformation and altering the airfoil geometry [26]. While, the technique adopted in the presented study from [26, 27] fixes the geometry and alter the transformation, calculated from the parameters that define the velocity distribution.

Moreover, in “multipoint” inverse design method the circle can be divided into any number of segments desired, Fig. 4 shows a four segments example. The segments S_1, S_2, S_3 and S_4 on the airfoil are mapped from a circle arc limits $\Phi_1, \Phi_2, \Phi_3, \Phi_4$. The circle arc limit begins at $\Phi = 0$ and

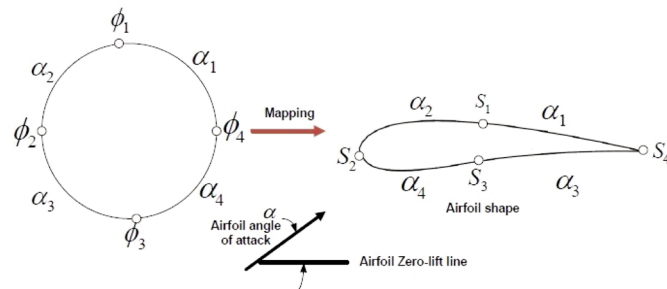


Figure 4. Schematic illustration of mapping a circle with four segments to an airfoil (adapted from [27])



Figure 5. 3D view of Airfoil UBD6166

finish at $\Phi = 60^\circ$. Further, the velocity distribution is prescribed for every segment along with the angle of attack at which the prescribed velocity distribution is to be attained [26]. The design angle of attack is positioned to the zero lift line. This method gives the designer a strong control and flexibility with any number of airfoil segments for specifying the desired velocity distribution and also the airfoil geometry or boundary layer development.

From multipoint inverse method the final airfoil profile, designated as, UBD6166 (Fig.5) is designed with maximum thickness of 6% at nearly $x/c = 16\%$ and the camber of 6% at $x/c = 42\%$. With the slight increase from the recommended thickness and camber for small HAWT airfoils i.e., 5% of thickness and camber, a short – shallow transition ramp is introduced over the upper surface at about $x/c = 16\%$ to 20%. It is emphasized that the span of the transition ramp is a compromise between the reduction of separation bubble, improvement in the operation range (C_{Lmax} , L/D) and the structural constraints. The aerodynamic performance of UBD6166 is detailed in later sections.

4. NUMERICAL STUDY OF AIRFOIL UBD6166

4.1. XFOIL study

For the initial aerodynamic performance of the airfoil, “Xfoil” [25] was used as a post-design viscous tool. In order to match this study with the wind tunnel conditions for future, the turbulence level in Xfoil was set to 1% and each airfoil in the present work was characterized in Xfoil by 230 panel nodes.

4.1.1. Performance comparison of UBD6166 with exiting airfoils

In the first instance, to set this study in a suitable global context the aerodynamic performance of airfoil UBD6166 was evaluated with existing low Re airfoils in Xfoil (Fig.6). Excluding the airfoil Davissm, which was designed for free flight application, all other airfoils used for comparison were designed for, or have been considered for small HAWT application. These airfoils include BW3, E387, FX63–137sm, S1223, SG6043, S1210 and S6062. Airfoil FX63–137sm, S1223 and S1210 were designed with a suction side transition ramp. Fig.6–Fig.9 represents the lift ($C_L - \alpha$), L/D ($L/D - \alpha$) and drag ($C_D - \alpha$) at $Re = 100\,000$. Relative thickness of each airfoil is also depicted for comparison. The coordinates of all the airfoils for comparison were collected from University of Illinois (UIUC) - Airfoil coordinates data base [20]. From Fig.6, airfoil Davissm produces the maximum L/D of 66.9 at $\alpha = 4^\circ$ and is highest compared to other chosen airfoils. Airfoil S1210 ranks second by producing L/D of 65 at $\alpha = 6^\circ$ and airfoil SG6043 generates $L/D = 63$ at $\alpha = 5^\circ$. Whereas Airfoil UBD6166 ranked fourth by producing maximum L/D of 62.7 at $\alpha = 4^\circ$. Other airfoils Fx63-137sm, E387, S1223, BW3 and S6062 produced $L/D = 60, 59, 58, 46$ and 43 at $\alpha = 5, 5, 6, 6$ and 4° respectively.

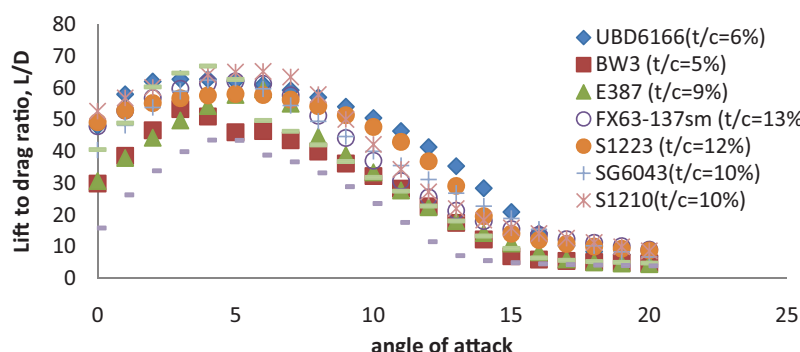
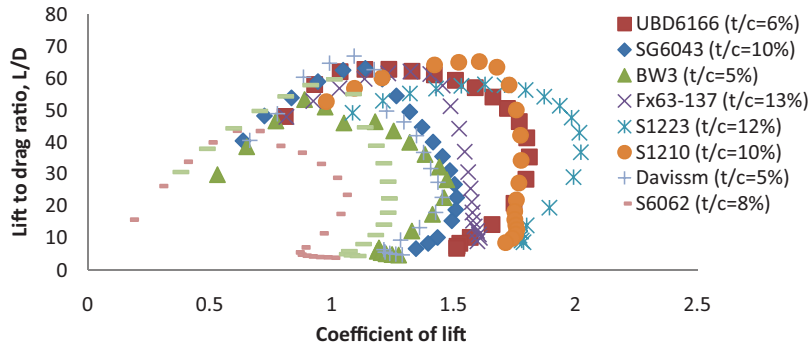
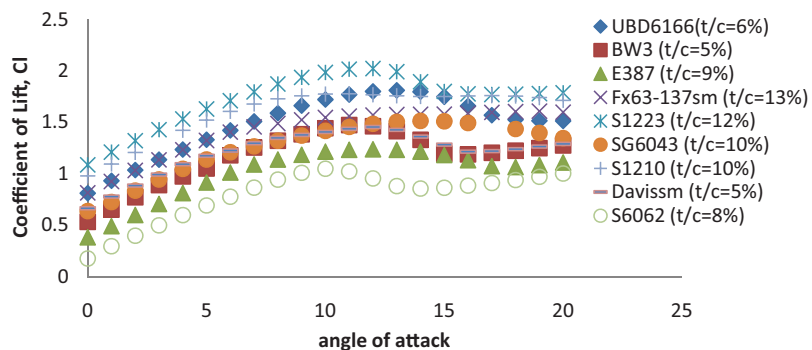
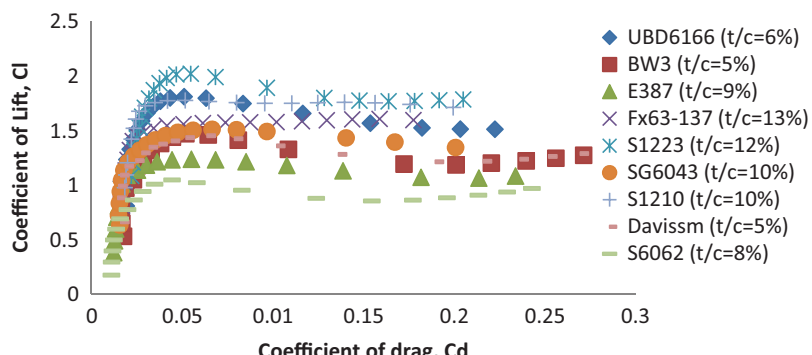


Figure 6. Lift-to-Drag plots (L/D ratio- α) various airfoils considered for small HAWT application at $Re = 100\,000$

Figure 7. Drag plots (L/D ratio- C_L) of airfoils considered for small HAWT application at $Re = 100\ 000$ Figure 8. Lift plots ($C_L - \alpha$) of various airfoils considered for small HAWT application at $Re = 100\ 000$ Figure 9. Drag polar plots ($C_L - C_D$) of airfoils considered for small HAWT application at $Re = 100\ 000$

The rapid degradation of L/D of thin airfoils such as Davissm and BW3 indicates a narrow operational α range over which low drag is attained (Fig.6). While, airfoils designed with suction side transition ramps like S1223 and Fx63-137sm and S1210 exhibit operating larger α range primarily due to the attached flow on the suction side. However along with the larger range, these airfoils may bring along the penalty of increased weight and consequently increased blade inertia. Airfoil UBD6166 with moderate thickness of 6% demonstrated increased aerodynamic efficiency- L/D against longer range of α as compared to existing airfoils.

Fig.7 represents L/D against C_L at $Re = 100\ 000$. Wider array of higher L/D over broad C_L envelope is seen for airfoil UBD6166. Further, the attached laminar flow which reciprocates in increased lift is revealed from Fig.8 C_L curves ($C_L - \alpha$) of the thick airfoils with transition ramp. Airfoil S1223 produces $C_{lmax} = 2.02$ at $\alpha = 12^\circ$ after which the aerodynamic lift drops rapidly indicating that airfoil has stalled. UBD6166 produces $C_{lmax} = 1.81$ at $\alpha = 13^\circ$. Airfoil S1210, Fx63-37sm and SG6043 shows soft stall behavior and depicts C_{lmax} of 1.77, 1.60 and 1.51 at $\alpha = 11, 19$ and 14° respectively.

Airfoil BW3 produces $C_{lmax} = 1.47$ at $\alpha = 11^\circ$ while airfoils Davissm, E387 and S6062 displayed C_{lmax} values of 1.45, 1.23 and 1.04 at $\alpha = 12, 12$ and 10° respectively. At $Re = 100\,000$ airfoils such as BW3 Davissm and S6062 displayed particularly narrow operational lift range for low drag (Fig.8) mainly because of their lower thickness. It is to note that all the airfoils considered for comparison were designed with specific and desired geometric and performance parameters in mind, and their direct comparison for single Re can be misleading. To infer, owing greatly to the higher aerodynamic performance with moderate thickness, UBD6166 airfoil shall benefit small HAWTs by reducing the rotor inertia and increasing the starting torque.

4.2. CFD Study

4.2.1. Computational domain

ICEM-CFD was employed for mesh generation. To get a fully developed and expanded flow, the length of the computational domain using a structured grid was 30 times that of chord length while width was 20 times the chord length. A quadrilateral mesh based on C-H grid topology was generated. Moreover, in order to ensure that the computed aerodynamic results are independent of the grid size, the density of grid was increased until negligible difference in solution is attained towards convergence. At the outset the coarse grid named as Grid 1 contained 100, 256 cells was used. Number of cells was increased to 180, 002 cells in Grid 2, whereas Grid 3 and Grid 4 contained 236, 250 and 300, 330 cells respectively. As shown in Fig.10, the difference in the aerodynamic performance results for $\alpha = 13^\circ$ in terms of lift is minor for all grids. Whereas, Grid 1 demonstrated drag values to be as twice compared to other grids. For, Grid 2 onwards differences in drag value were negligible. Thus, refined Grid 3 with 236, 250 cells was adopted for numerical experimentation. To capture the transition, flow separation and most importantly the LSB, the mesh density was increased in the region of boundary layer for all grids. The adjacent surface wall node was satisfied with $y^+ < 1$. This was essential for precise simulation of the boundary layer flows and the coupled lift and drag forces of airfoils. Dense grids were placed near the leading and trailing edges because of the steepest gradients. The transition in mesh size was kept smooth as possible for numerical accuracy and the mesh density was kept progressively coarser in the far-field area as the flow gradients approaches zero. Inlet boundary conditions were set as velocity inlet and pressure outlet was selected for outlet boundary conditions. The domain and meshed airfoil are depicted in Fig.11.

4.2.2. Solver settings in ANSYS-FLUENT

The solver was set for steady state. To solve the coupling problem between the pressure in momentum equations and velocity components, the SIMPLE algorithm was employed and second order upwind spatial discretization was used. Whereas spatial gradient was chosen as least squares cell based. For boundary conditions at inlet, intermittency γ was taken as 1 and Turbulence intensity was put to $\leq 1\%$ to produce conditions similar to that of a wind tunnel. Velocity at inlet was specified to achieve the desired Re . Further, desired angle of attack was attained by rotating the mesh and for convergence criteria residual target values were set to 10^{-6} . The angle of attack was increased gradually to capture the movement of possible separation bubble and stall angle precisely.

4.2.3. Turbulence model

The transition SST (Shear Stress Transport) model is used in this study in order to incorporate turbulence. Transition SST is a four equation turbulence model that combines SST $k-\bar{\epsilon}$ transport

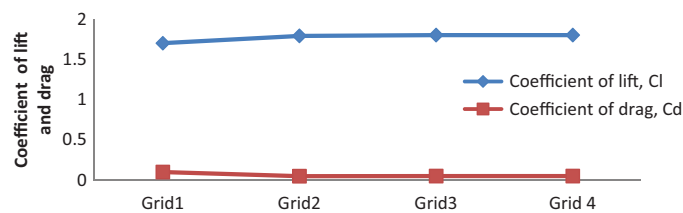


Figure 10. Coefficient of lift and drag for UBD6166 airfoil at $\alpha = 13^\circ$ from different grid sizes

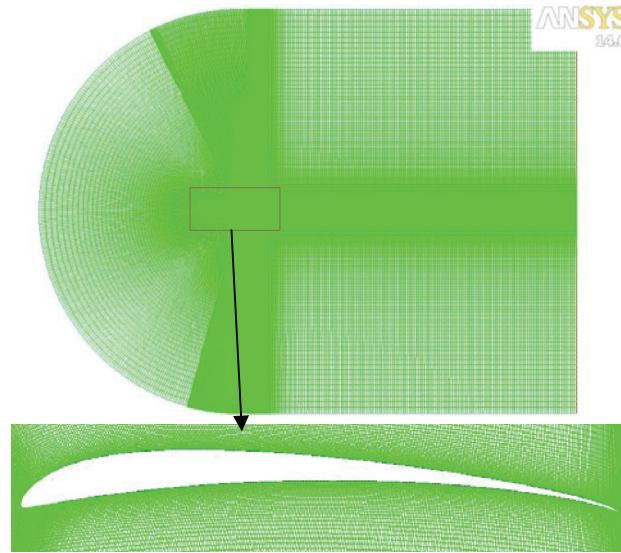


Figure 11. UBD6166 structured grid mesh

equations with two additional transport equations, one for intermittency γ and second for transition Reynolds number Re_{θ_t} which is in terms of the momentum – thickness Reynolds number Re_{θ} . γ activates the production term of turbulent kinetic energy downstream of the transition point in the boundary layer and Re_{θ_t} captures the nonlocal effect of the turbulence intensity, as shown in [21]. Therefore this model is also known as $\gamma - Re_{\theta}$ model. In general, this hybrid turbulence model associates transition modeling with experimental data. The transport equation for intermittency and transition momentum thickness according to [21] are given as:

$$\frac{\partial(\rho\gamma)}{\partial t} + \frac{\partial(\rho U_j \gamma)}{\partial x_j} = P_{\gamma 1} - E_{\gamma 1} + P_{\gamma 2} - E_{\gamma 2} \quad (5)$$

$$\frac{\partial(\rho \tilde{R}e_{\theta_t})}{\partial t} + \frac{\partial(\rho U_j \tilde{R}e_{\theta_t})}{\partial x_j} = P_{\theta_t} + \frac{\partial}{\partial x_j} \left[\sigma_{\theta_t} (\mu + \mu_t) \frac{\partial \tilde{R}e_{\theta_t}}{\partial x_j} \right] \quad (6)$$

The constants in intermittency equations are taken as original provided in ANSYS [22] which are $C_e = 1.0$; $C_a = 2.0$; $C_{e2} = 50$; $C_{a2} = 0.06$; $\square_f = 1.0$. The constants for Reynolds number momentum thickness given by ANSYS [22] are $C_{\theta_t} = 0.03$; $\square_{\theta_t} = 2.0$. These values were originally obtained from experiments on boundary layer transition flat plate. Thus, modified values of $C_{\theta_t} = 0.02$ and $\square_{\theta_t} = 3.0$ based on simulations of low Re flow on circular arc airfoils [23] are used in the present study to determine the onset length of transition.

4.3. CFD results

The pressure distribution (C_p) over airfoil surfaces against the chord length from the SST-transition model is shown in Fig. 12(a) – (f) for stall angle $\alpha \approx 13^\circ$ at $Re = 60\,000, 100\,000, 200\,000, 300\,000, 400\,000$ and $500\,000$. Concave type pressure recovery, as prescribed is seen over the suction side of the airfoil. Further, the corresponding Xfoil results are also plotted for comparison. Close correlation is revealed between C_p from Xfoil and SST-transition pressure distributions. Suction peaks of -4.7 and -3.8 are noted from Xfoil and SST-transition correspondingly. Whereas, Suction peaks of -5.0 and -4.8 are observed for $Re = 100\,000$ for Xfoil and SST-transition respectively. Suction peak of -5.5 and -5.0 , -6.47 and -5.8 , -7.09 and -6.51 , -7.31 and -6.8 are observed for $Re = 200\,000, 300\,000, 400\,000$ and $500\,000$ for Xfoil and SST-transition respectively. The increase in magnitude of the suction peak with increasing Re reveals the growth in the pressure recovery which is generally defined by the airfoil thickness and the pitching moment constraints. Moreover from SST-transition pressure distribution plots no suction spike is observed at the leading edge.

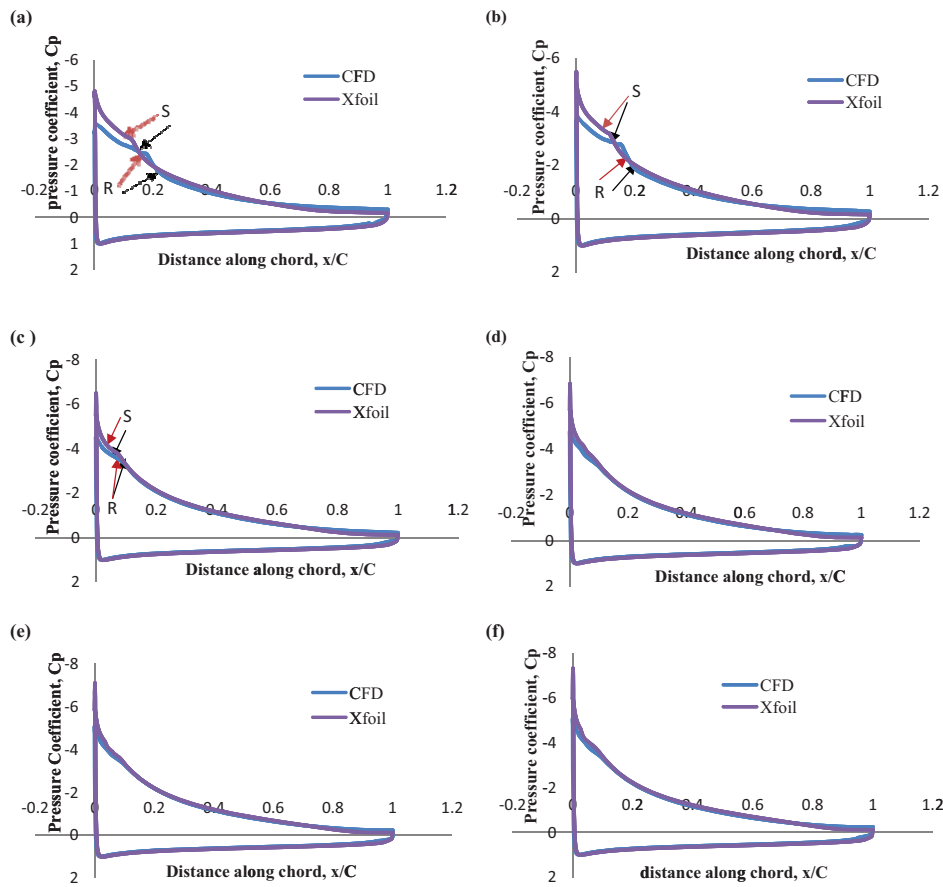


Figure 12. Comparison of Pressure distribution from Xfoil and SST-transition, over airfoil UBD6166 at $\alpha = 13^\circ$ for (a) $Re = 60\ 000$ (b) $100\ 000$ (c) $200\ 000$ (d) $300\ 000$ (e) $400\ 000$ and (f) $500\ 000$

Further at low Re range in fig 12(a)–(c) the LSB is associated with a pressure plateau at the suction side. The separation point and reattachment points are labeled as “S” and “R” respectively. In comparison between SST-transition with Xfoil, a discrepancy can be seen in location of the LSB. For the remaining Re the flow remain attached to the airfoil surface and the pressure recovers smoothly. LSB at the lower Re range are reported to be common for most low Re airfoils and it represents the transition forcing mechanism [9]. Such mechanism is seen the present study as well. Moreover, as shown by the pressure distribution plots, LSB tends to shift upstream with increasing Re , alongside the size of the LSB became slightly shorter with increasing Re as well. With increasing α the length of the LSB reduces and moves towards the leading edge of the airfoil. A summary of location of separation and reattachment points at various α computed from of SST-transition is depicted in Fig.13.

In Fig.13 flow separation and reattachment points along the airfoil’s chord length are plotted as a function of angle of incidence for Re 600 00, 100 000 and 200 000. At Re 60 000. For lower range of angle of incidence that is $\alpha \geq 2^\circ$, the laminar boundary layer remains attached over suction surface area and leaves the airfoil smoothly at trailing edge. As the angle of incidence increases the separation point moves further upstream followed by transition without reattachment. It is found from the calculations that the bubble has developed into the far wake. Further at $\alpha \approx 3^\circ$, under the influence of an adverse pressure gradient the laminar boundary layer separates at $x/c \approx 0.42$, and reattaches to the airfoil surface at $x/c = 0.46$ forming LSB. Additionally, the turbulent boundary layer also separates ahead of the trailing edge. Further from $\alpha \approx 4^\circ$ till $\alpha \approx 14^\circ$, the bubble moved further towards the leading edge. The movement of transition towards leading edge is also revealed from increase in turbulent kinetic energy (TKE) near the leading edge in Fig.16 (a) at $\alpha = 10^\circ$. At $\alpha \approx 15^\circ$ the bubble elongated and followed by

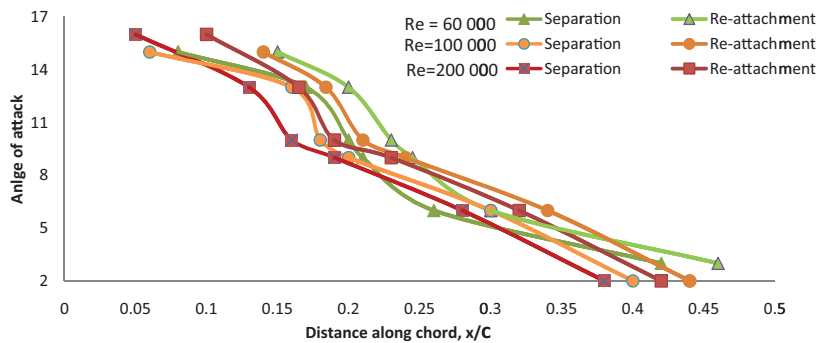


Figure 13. Separation and Reattachment of flow over suction side of airfoil at $Re = 60\,000$, $100\,000$ and $200\,000$ predicted by the SST-transition model

turbulent boundary layer separation. Further the reattachment of the separated turbulent flow happens closer to the trailing edge which mainly explains the gradual stall in $C_L - \alpha$ plot. With additional increase in α no reattachment of the turbulent flow is seen. Similar pattern of LSB movement is seen for $Re = 100\,000$ and $200\,000$ except that the separation and reattachment started to occur from at $\alpha \approx 2^\circ$. Moreover at $Re = 200\,000$ LSB is still observed till $\alpha \approx 16^\circ$. Furthermore, for a wind turbine application examining the influence of airfoils surface roughness is also very essential. From $C_L - \alpha$ alpha plots, drag polar plots and the LSB movement it is revealed that maximum lift for UBD6166 occurs while turbulent flow is covering about up to 80% of the airfoils suction surface. This suggests that the airfoil is either insensitiveness to roughness or the roughness effects are diminished due the higher turbulence level. However, thorough study with fixed transition and surface roughness is recommended for more detailed performance evaluation.

From Fig.15 (a)–(c) the summary of lift and drag coefficient of UBD6166 as a function of angle of attack and a lift-drag polar plot are shown. These plots are the result of integration of surface pressure distribution around the 2D airfoil computed in Fluent using the SST-transition model. At $Re = 60\,000$, $100\,000$ and $200\,000$ aerodynamic lift smoothly increases till $\alpha \geq 9^\circ$. This shows that the laminar boundary layer remains attached to the airfoil surface and departs at the trailing edge to satisfy the Kutta condition (Fig.15.a). Due to very minimal size of LSB no clear drag knee (which represents LSB) is observed in the drag polar plot (Fig.15.c).

Further, the deficit in aerodynamic lift is associated with separated flow. However, the subsequent flow remains attached to the airfoil till the flow separates at the trailing edge. For $Re = 400\,000$ and $500\,000$ the stall angle has moved up to $\alpha = 15^\circ$. Additionally, decrease in drag (Fig.15.b) with increasing Re is clearly associated with higher lift. At higher Re range, no LSB is seen and consequently lower drag is produced. As indicated from the results that the transition ramp provided surpassed the disastrous effects of LSB. In addition UBD6166 also encourages docile stall characteristics.

The phenomenon of flow reversal inside the LSB is clearly revealed from the plots of velocity vectors in Fig.14 (a)–(c) for $Re = 60\,000$, $100\,000$ and $200\,000$. These snapshots further shows that LSB tends to downsize in height with increasing Re . LSB at the given Re might be diminished with increasing transition ramp size, which however may bring along the penalty of unwanted thickness and in other words a more costly machine. From Fig.14 (d)–(f) with the help of transition ramp no separation is seen over the upper side of the airfoil at $Re = 300\,000$, $400\,000$ and $500\,000$ and the flow remains attached. For all the Re considered in this study the flow separation begins at the trailing edge and proceeds forwards on the airfoil with incidence. Transition from laminar to turbulent flow over suction side of airfoil is shown in the turbulent kinetic energy contours (TKE) in Fig.16 (a)–(b) for $\alpha = 13^\circ$ and $Re = 60\,000$ and $500\,000$. For $Re = 60\,000$ the TKE is minimum in the laminar flow section i.e. towards the leading edge section of the airfoil. Increased TKE represents the transition in LSB and helps the flow to overcome adverse pressure gradients and its reattachment to the airfoil surface. At $Re = 500\,000$ the transition ramp triggers the transition from laminar to turbulent flow at the leading edge and no LSB is seen.

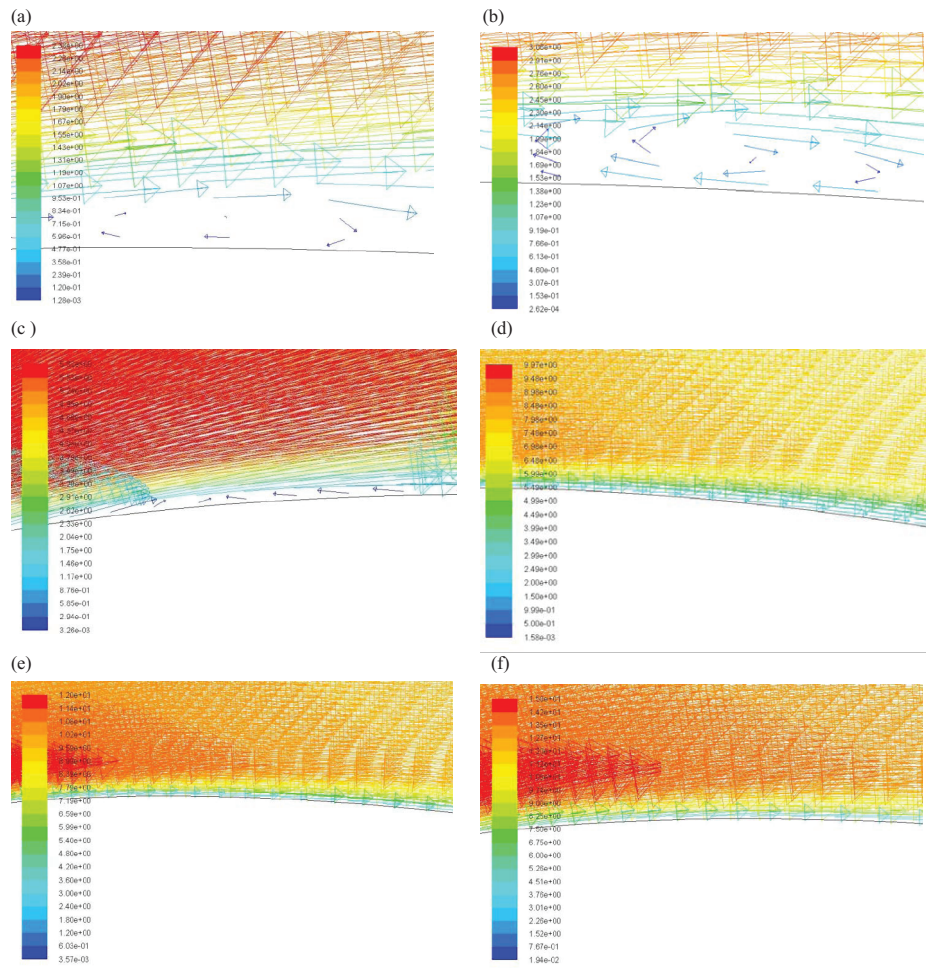


Figure 14. Velocity vectors on suction side of airfoil UBD6166 at $\alpha = 13^\circ$ predicted by SST-transition model for (a) $Re = 60\,000$ (b) $100\,000$ (c) $200\,000$ (d) $300\,000$ (e) $400\,000$ (f) $500\,000$

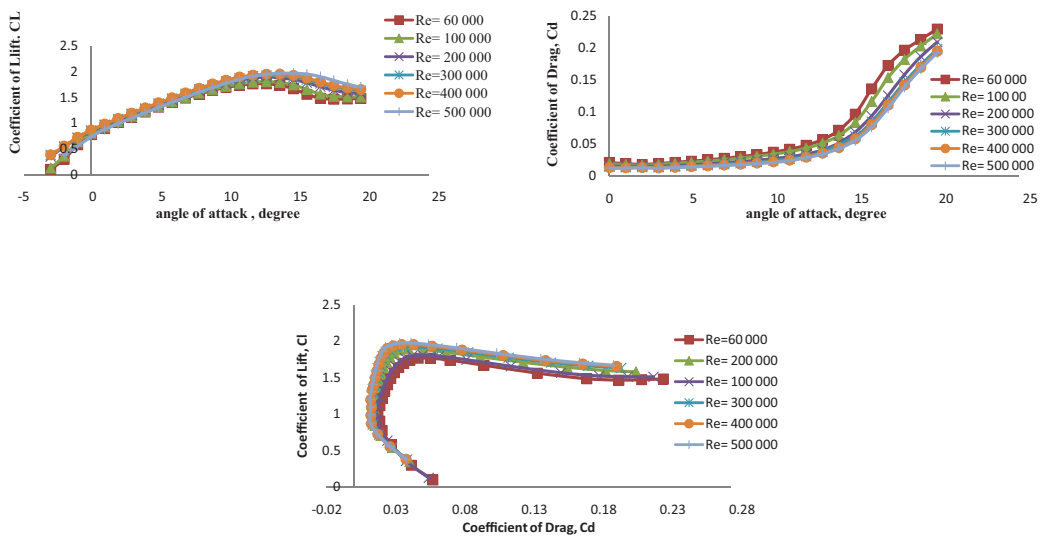


Figure 15. (a) Lift plots ($C_L - \alpha$) for airfoil UBD6166 at various Reynolds numbers (b) Drag plots ($C_D - \alpha$) for airfoil UBD6166 at various Reynolds numbers (c) Drag polar plots ($C_L - C_D$) of UBD6166 at various Reynolds number

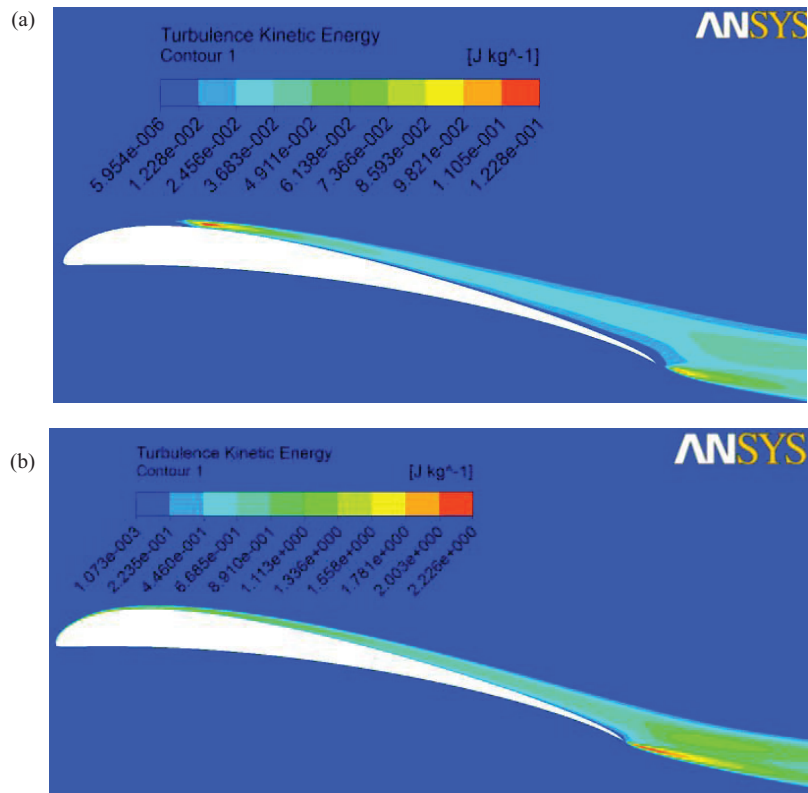


Figure 16. Turbulent kinetic energy contour around airfoil UBD6166 at $\alpha = 10^\circ$ for $Re =$ (a) 60 000 (b) 500 000

5. MULTI-OBJECTIVE OPTIMIZATION

5.1. Methodology

Wind turbine blades are often optimized with a single objective i.e., for maximum power. This results in poor starting performance for small HAWT [2, 12]. An evolutionary algorithm based multi-objective optimization technique is adapted in the present study to maximize both the power and the self starting performance. It produces best fitted offspring by random selection of parents and sharing of genetic material (in this case the chord and twist of the blade elements) for solving the optimization problems. Moreover, it begins with an initial population of blades which are randomly assigned as chord and twist. The next generation is obtained by mutating the elements of random selection of parents. Weighted difference of two selected parents is added into the third member so-called mutant vector. A binomial crossover between trial vector and mutant vector forms the final trial vector with the best element. Classical blade element momentum theory is employed to find the C_p where customized blade element gives starting, meanwhile each blade element consists of a gene with chord and twist properties, see [5] for details. The behavior of DE may vary depending on the population size and crossover probability constant. The fitness function is determined as:

$$\text{Fitness } (c_i) = a \frac{C_p(C_i)}{\max(C_p)} + \frac{(1-a)(\min(T_s))}{T_s - (C_1)} \quad (7)$$

Where, C_p and inverse of starting time, T_s are the two objective to be optimized. Further, the mixing of starting and C_p in terms of importance is set by the value of weighting factor a which controls the relative power efficiency and the starting time. Varying the value of a allows mapping the “Pareto front” of optimal blade designs, such that lower weighting factor will produce early starting blades and higher will give superior performing blades. This Pareto front defines the optimal blade for a two dimensional optimization. The “non-dominated” blades are the elements of this Pareto front and blade designers have to choose one blade on the Pareto front, since there is no *one* best blade in two-dimensional optimization that is, essentially, a trade off. The initial population was set to 2000, and number of generations to be evolved was 400, whereas no member of population is permitted to live for more than 20 generations. Crossover step is the mixing of parental genetic

material in forming the offspring's and is taken as 0.1. The results for C_p and starting were obtained using 15 blade elements.

The starting time, T_s is identified when the desired starting tip speed ratio approached. In this study its set to 1.0. The power producing tip speed ratio is set to 6.10. Rotor consisting of 3 blades, each of 1.06 m is considered. Further, starting and power producing wind speed was taken as 5 and 10 m/s respectively. The minimum chord length of blade is 0.01 and maximum is 0.2, both as a fraction of the blade radius, while minimum and maximum twist is taken as 4 and 25° correspondingly. Rotor inertia for the chosen generator is 0.006 kgm². The chosen permanent magnet generator chosen had the rated power of 754W at 550rpm. Further, Two cases were considered to calculate the starting time and power coefficient. In the first case a generator without resistive torque i.e., $Q_r = 0$ is considered where as maximum resistive torque of $Q_r = 0.5$ is considered for the second case. Both cases were explored with variation of weighting factor, starting from $a = 0.7$ to 0.8 and 0.9. The lift and drag coefficients for all α and Re are interpolated from the simulation data from Ansys-Fluent.

5.2. Multi-objective optimization results

As anticipated, lower values of the weighing factor a gave early starting time and the higher values produced blades with greater C_p . In the absence of the generator resistive torque $a = 0.7$ resulted with $C_p \approx 0.46$ at starting time ≈ 1.2 seconds, whereas $a = 0.8, 0.9$ produced $C_p \approx 0.48$ and 0.5 at starting time of 1.53 and 1.75 seconds respectively. It can be observed that a slight reduction in C_p can reduce the starting time. The second case as stated earlier is to take into account the maximum cogging torque from generator, i.e., $Q_r = 0.5$. With the introduction of cogging torque, in Fig.17, a shift in the Pareto front is observed. With $Q_r = 0.5$ and $a = 0.7$, $C_p \approx 0.475$ at starting time ≈ 3.1 seconds, where as $a = 0.8, 0.9$ produces $C_p \approx 0.49$ and 0.498 at starting time ≈ 3.34 and 3.9 seconds respectively. As compared to airfoil SG6403 designed for low Re application, UBD6166 airfoil improve the performance of a 2m small HAWT in terms of starting and energy capture. The evolved chord and twist distributions for averaged non-dominated blades are shown in Fig.18. It can be noted that fast starting blades, which are products of lower values of a , have increased chord at hub region along with slight increase in twist whereas the tip regions mostly remain the same as for blades with high C_p . However, the changes in hub regions with changing values of a indicate the vital role in starting performance. It is clear that hub region contributes much torque in starting rather than power production. The impact of resistive torque is clearly noticeable from the change in chord and twist. Also, the C_p has maximized compared to the first case and delay in starting is no-doubt result of the resistive torque from the generator. In both cases, the algorithm found the optimal blades have increased chord and twist at the hub.

In two dimensional optimization, the final blade completely rely upon the designer to chose the appropriate value of a from the parent front which outcomes in the optimal superior blade. Using UBD6166 airfoil and $Q_r = 0$, blades design from weighing factor $a = 0.9$ would be suitable. Moreover for $Q_r = 0.5$, $a = 0.7, 0.8$ and 0.9 are appropriate weighing factors. In an ideal situation where maximum C_p is the key objective the blade design with weighting factor of $a = 0.9$ will be chosen. But as the starting performance is concerned, $a = 0.8$ improved the starting time by 17%

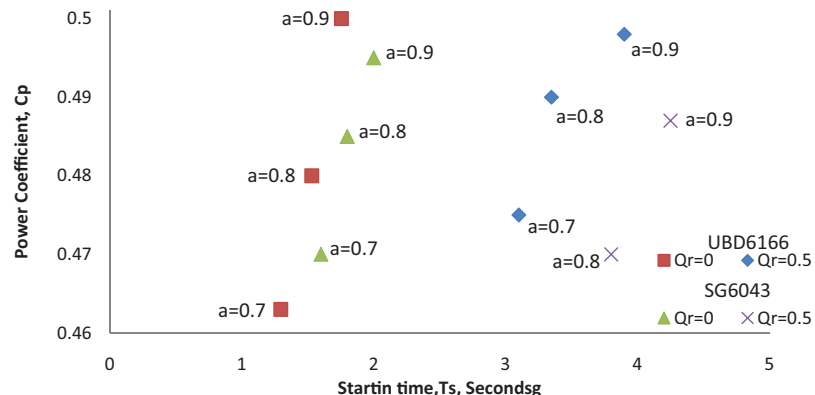


Figure 17. Paretofront comparison of the blade design using airfoil UBD6166 and SG6043 from [5]

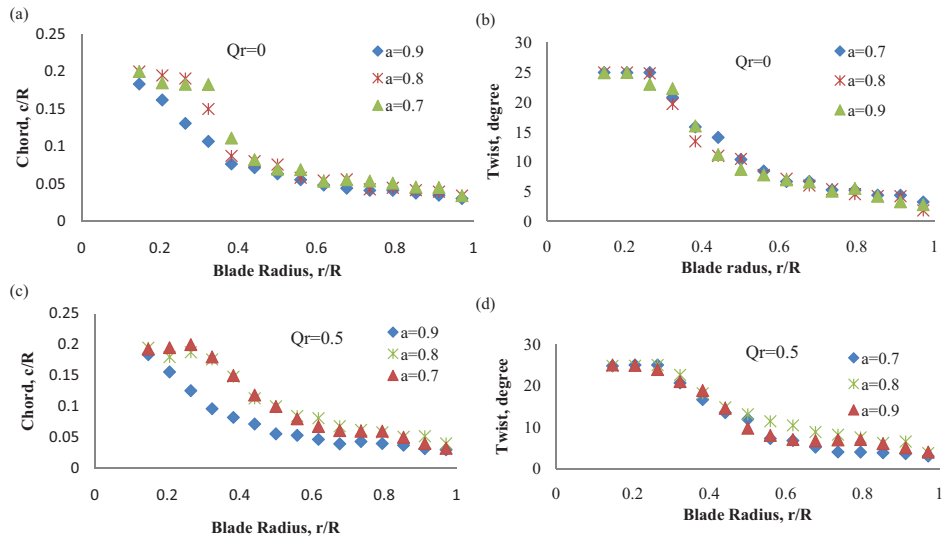


Figure 18. (a) (b) (c) (d) Evolved chord and twist distributions for averaged non-dominated blades

with nearly 2% reduction in C_p and $a = 0.7$ reduced the starting time by 25% with 5% C_p loss. Hence, blade design with weighting factor of $a=0.8$ is chosen by the author as the best compromise between the starting and the C_p .

6. CONCLUSION

This paper describes the design of a new airfoil profile “UBD6166” that can improve the self starting and power capture of small HAWTs at low wind speed. This was accomplished by designing the airfoil with optimum transition ramp via multipoint inverse design method and the optimization technique for the rotor design. The goal of improving the aerodynamic performance by controlling the LSB via optimum transition ramp was accomplished. Airfoil UBD6166, owing largely to the higher aerodynamic performance with moderate thickness, shall benefit small HAWTs by reducing the rotor inertia and increasing the starting torque. From two dimensional optimization, fast starting blades were found to have increased chord at hub region along with slight increase in twist whereas the tip regions mostly remain the same. Moreover, the two dimensional optimization is based upon the tradeoff between maximizing one objective function while reducing the other; the desired optimal design can be chosen from the Pareto front.

AKNOWLEDGEMENTS

The authors are thankful to the Universiti of Brunei Darussalam for providing necessary funding for this research under the S&T Research Grant. We would also like to thank Dr. David Wood and Mohamed Arif bin Mohamed from University of Calgary, Department of Mechanical and Manufacturing Engineering, Calgary, Alberta, Canada for guidance and support in ANSYS-CFD and MATLAB.

REFERENCES

- [1] Global Wind Energy Council, retrieved from www.GWEC.net, 2013.accesed on 15/02/2014.
- [2] International standard, IEC 61400–2, wind turbines- part 2: small wind turbines, Edition3, 2013–12.
- [3] Clausen, P.D. and Wood, D.H., Research and development issues for small wind turbines, *Renewable Energy*, 1999, 16, 922–927.
- [4] Mathew, S., Philip,G.S., *Advances in wind energy conversion technology*, Springer-Verlag, Berlin., 2011.
- [5] Wood, D., *Small Wind Turbines, Analysis, Design, and Application*, Green Energy and Technology, Springer. 2011.

- [6] Miley, S.J., *A catalog of low Reynolds number airfoil data for wind turbine applications*, report, RFP-3387, UC-60.
- [7] Giguère, P., Selig, M.S., Low Reynolds number airfoils for small Horizontal axis wind turbines. *Wind Engineering*, 1997, 21, 367–380.
- [8] Tangler, J.L., *The evolution of rotor and blade design*. NREL report, 2000.
- [9] Giguère, P., Selig, M.S., New airfoils for small horizontal axis wind turbines, *Journal of Solar Energy Engineering*, 1998, 120, 108–114.
- [10] Selig, M.S., Guglielmo, J.J., Broeren, A.P., Giguère, P., *Summary of low-speed airfoil data*, SOARTECH publications-USA, 1995, volume 1.
- [11] Selig, M.S., Lyon, C.A., Giguère, P., Ninham, C.P., Guglielmo, J.J., *Summary of low-speed airfoil data*, SOARTECH publications-USA, 1996, volume 2.
- [12] Lyon, C.A., Broeren, A.P., Giguère, P., Gopalarathnam, A., Selig, M.S., *Summary of low-speed airfoil data*, SOARTECH publications-USA, 1997, volume 3.
- [13] Selig, M.S., Macgranahan, B.D., Wind tunnel aerodynamic tests of six airfoils for use on small wind turbines. *Journal of Solar Energy Engineering*, 126, 986–1001.
- [14] Lissaman, P.B.S., Low-Reynolds-number-airfoils, *Annual review Fluid mechanics*, 1983, 15, 233–239.
- [15] Shah, H., Lim, C.M., Mathew, S., Low Reynolds number airfoil for small horizontal axis wind turbine blades, *Sustainable future energy 2012 and 10th SEE FORUM*, 2012, Brunei Darussalam.
- [16] Tanglers, J.L., Somers, D.M., “NREL airfoil families for Small HAWT”. AWEA, 1995, Washington.
- [17] Drela, M., Low Reynolds-Number Airfoils Design for the M.I.T. Daedalus Prototype: A case study, *Journal of Aircraft*, 1988, 25, 724–732.
- [18] Selig, M.S., Lecture notes on Low Reynolds number airfoil design, 2003, *VKI lecture series*.
- [19] Genc, M.S., *Low Reynolds Number Aerodynamics and Transition*., INTECH, 2012.
- [20] University of Illinois (UIUC)- Airfoil coordinates data base, UIUC Applied Aerodynamics group, Department of Aerospace Engineering. <http://www.ae.illinois.edu/m-selig/ads.html>.
- [21] Menter, P.R., Langtry, R., Voker, S., Transition Modelling for General Purpose CFD Codes, *Flow, Turbulence and Combustion* 2006, 77, 277–303
- [22] ANSYS. ANSYS academic research, *Fluent theory guide*. Technology Dr. Canonsburg, PA 15317, 2011.
- [23] Fagberno, K., Mohammad, M.A., Wood, D.H., Computational modeling of Windmill blades at high solidity, *Energy for Sustainable Development* (to appear).
- [24] Horton, H. P, *Laminar Separation Bubbles in Two and Three Dimensional Incompressible Flow*, PhD thesis, Queen Mary College, University of London, 1968.
- [25] Drela, M., *XFOIL : An Analysis and Design System for Low Reynolds Number Airfoils*, Low Reynolds Number Aerodynamics, lecture Notes in Engineering, Springer, 54, 1989, 1–12.
- [26] Selig, M.S., Maughmer, M. D., A Multi-point Inverse Airfoil Design Method Based on Conformal Mapping, *AIAA Journal*, 1992, 30–5, 1162–1170.
- [27] Selig, M.S., Maughmer, M. D., Generalized Multipoint Inverse Airfoil Design, *AIAA Journal*, 1992, 30–11, 2618–2625.

